INVESTIGATING SLIM DISK SOLUTIONS FOR HLX-1 IN ESO 243-49

O. GODET[1,2], B. PLAZOLLES[1,2], T. KAWAGUCHI[3], J.-P. LASOTA[4,5], D. BARRET[1,2], S. A. FARRELL[6,7],
V. BRAITO[6], M. SERVILLAT[8], N. WEBB[1,2], AND N. GEHRELS[9]

[1] Institut de Recherche en Astrophysique et Planétologie (IRAP), Université de Toulouse, UPS, 9 Avenue du colonel Roche, 31028 Toulouse Cedex 4, France
[2] CNRS, UMR5277, 31028 Toulouse, France
[3] Center for Computational Sciences, University of Tsukuba, 1-1-1 Tennodai, Tsukuba, Ibaraki 305-8577, Japan
[4] Institut d'Astrophysique de Paris, UMR 7095 CNRS, UPMC Université Paris 06, 98bis Boulevard Arago, 75014 Paris, France
[5] Astronomical Observatory, Jagiellonian University, ul. Orla 171, 30-244 Krakow, Poland
[6] Department of Physics and Astronomy, University of Leicester, University Road, Leicester LE1 7RH, UK
[7] Sydney Institute for Astronomy, School of Physics A29, The University of Sydney, NSW 2006, Australia
[8] Harvard-Smithsonian Center for Astrophysics, 60 Garden Street, MS-67, Cambridge, MA 02138, USA
[9] NASA/Goddard Space Flight Center, Greenbelt, MD 20771, USA

ABSTRACT

The hyperluminous X-ray source HLX-1 in the galaxy ESO 243-49, currently the best intermediate-mass black hole (BH) candidate, displays spectral transitions similar to those observed in Galactic BH binaries, but with a luminosity 100–1000 times higher. We investigated the X-ray properties of this unique source by fitting multi-epoch data collected by *Swift*, *XMM-Newton*, and *Chandra* with a disk model computing spectra for a wide range of sub- and super-Eddington accretion rates assuming a non-spinning BH and a face-on disk ($i = 0°$). Under these assumptions we find that the BH in HLX-1 is in the intermediate-mass range ($\sim 2 \times 10^4 \, M_\odot$) and the accretion flow is in the sub-Eddington regime. The disk radiation efficiency is $\eta = 0.11 \pm 0.03$. We also show that the source does follow the $L_X \propto T^4$ relation for our mass estimate. At the outburst peaks, the source radiates near the Eddington limit. The accretion rate then stays constant around $4 \times 10^{-4} \, M_\odot \, \mathrm{yr}^{-1}$ for several days and then decreases exponentially. Such "plateaus" in the accretion rate could be evidence that enhanced mass-transfer rate is the driving outburst mechanism in HLX-1. We also report on the new outburst observed in 2011 August by the *Swift* X-Ray Telescope. The time of this new outburst further strengthens the ~ 1 year recurrence timescale.

Key words: accretion, accretion disks – black hole physics – galaxies: individual (ESO 243-49) – methods: data analysis – X-rays: individuals (HLX-1)

Online-only material: color figures

1. INTRODUCTION

Ultraluminous X-ray sources (ULXs) are defined as off-nucleus extragalactic sources showing X-ray luminosity exceeding $3 \times 10^{39} \, \mathrm{erg \, s^{-1}}$ assuming isotropic emission (see Roberts 2007). Even if their nature is still in dispute, it is likely that their huge luminosity is produced by accretion of matter onto a black hole (BH). Three explanations for their nature have been considered. (1) ULXs may be X-ray stellar mass BH binaries (BHBs) similar to those observed in our Galaxy, but in a more extreme version of the very high state (e.g., Remillard & McClintock 2006), the ultraluminous or wind-dominated state (e.g., Gladstone et al. 2009). In such states, the source would be able to radiate above the Eddington limit. It is still to be understood why this ultraluminous state is so rarely observed in X-ray binaries. (2) King et al. (2001) proposed that the emission of ULXs is highly anisotropic. In this case, the requirement to have super-Eddington emission is alleviated. The nature of this anisotropy could be due to either geometrically thick disks funneling the X-ray photons produced in the inner parts of the accretion disks (King 2009) or due to relativistic beaming of a jet or strong outflow. However, the discovery of several optical and radio nebulae around ULXs (e.g., Pakull & Grisé 2008) and quasi-periodic oscillations in M82 X-1 (Strohmayer & Mushotzky 2003) argue against strong beaming. (3) The final and the most exciting explanation is that some ULXs are accreting intermediate-mass BHs (IMBHs) with masses ranging from $\sim 100 \, M_\odot$ to

$\sim 10^5 \, M_\odot$ (e.g., Colbert & Mushotzky 1999). The existence of such IMBHs will naturally alleviate the need for super-Eddington emission. It is clear now that the IMBH interpretation is not valid to explain the ULX population as a whole (see, e.g., Roberts 2007). However, the most luminous ULXs, the so-called hyperluminous X-ray sources (HLXs; Gao et al. 2003) with X-ray luminosities above $10^{41} \, \mathrm{erg \, s^{-1}}$, are good candidates. Finding convincing evidence for the existence of IMBHs is important for the growth of supermassive BHs via mergers or accretion episodes (e.g., Micic et al. 2007), dark matter studies (e.g., Fornasa & Bertone 2008, but see also Bringmann et al. 2009), cosmology (e.g., Trenti & Stiavelli 2007), and gravitational wave detection (e.g., Matsubayashi et al. 2004; Amaro-Seoane & Santamaría 2010).

Farrell et al. (2009) reported the serendipitous discovery of a ULX candidate 2XMM J011028.1–460421, referred to hereafter as HLX-1, located in the outskirts of the edge-on spiral galaxy ESO 243-49 at a redshift of 0.0224 (Wiersema et al. 2010). From its maximum luminosity reaching $\sim 1.3 \times 10^{42} \, \mathrm{erg \, s^{-1}}$ at peak and assuming that the source luminosity reached up to 10 times the Eddington limit (L_{Edd}), Farrell et al. (2009) derived a BH mass of more than $500 \, M_\odot$. HLX-1 is so far the best candidate to harbor an IMBH. Apart from its extreme luminosity, which has been observed many times over the past 3 years by different X-ray satellites (*Swift*, *XMM-Newton*, and *Chandra*), HLX-1 is unique among other ULXs because it is the only one for which clear spectral hysteresis similar to those observed in Galactic BHBs (GBHBs) are seen. Indeed,
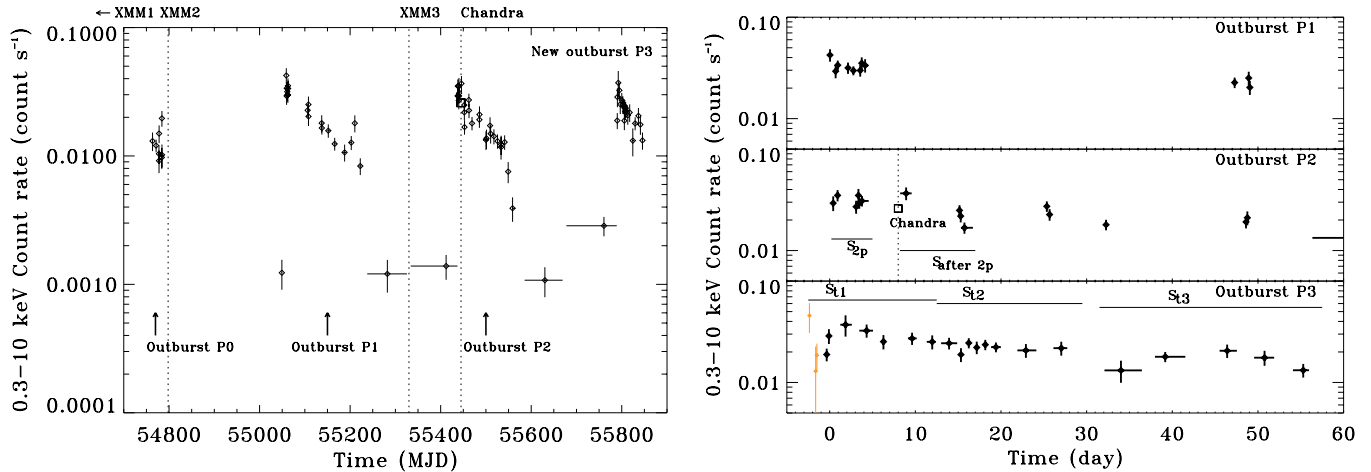
Figure 1. *Swift*–XRT photon counting 0.3–10 keV light curve of HLX-1 up to 2011 September 5. The *Swift*–XRT light curve was obtained using the *Swift*–XRT light-curve generator web interface with a binning of at least 60 counts per bin (Evans et al. 2009). Left: the vertical dotted lines mark the times of the *XMM-Newton* and *Chandra* observations. Right: close-up view of the X-ray light curve around the outburst peaks P1, P2, and P3. The zero time corresponds to the time when we first observed a re-brightening from the source (P1 = 2009 August 16 and P2 = 2010 August 29) and the peak of the outburst P3 (2011 August 15). The square on the middle panel is the predicted on-axis *Chandra* count rate into the 0.3–10 keV *Swift*–XRT energy band. Bottom panel: the thin points were obtained using a lower temporal binning for data from MJD = 55,788 to MJD = 55,790.

(A color version of this figure is available in the online journal.)

Servillat et al. (2011), using *XMM-Newton*, *Chandra*, and *Swift* data, confirmed the results presented in Godet et al. (2009) that HLX-1 underwent transitions from the high/soft state to the low/hard state. The *Swift* X-Ray Telescope (XRT) light curve so far covers four outbursts from 2008 to 2011 (hereafter P0, P1, P2, and P3—see Figure 1). While we had only one observation in 2008 October during the P0 outburst, the P1 and P2 outbursts display well-sampled fast-rise/exponential-decay-like temporal profiles. Thanks to our dedicated *Swift*–XRT target of opportunity, we caught the rise of the P3 outburst from 2011 August 15 (Godet et al. 2011). A precursor could be seen prior to the P3 outburst peak in Figure 1. Two re-flare events are also visible during the P1 and P3 outbursts. The outbursts appear to be separated by a recurrence timescale of nearly a year. Recently, Lasota et al. (2011) interpreted the X-ray light curve as the result of enhanced mass-transfer rate onto a pre-existing accretion disk around an IMBH, when an asymptotic giant branch star orbiting along an eccentric orbit with a period of ∼1 year is tidally stripped near periastron.

In order to further investigate the nature of this unique source, it is essential to put some constraints on the accretion flow and the BH mass. Lower and upper limits from radio, optical, and X-ray observations have been derived (see Wiersema et al. 2010; Servillat et al. 2011; Webb et al. 2012). Davis et al. (2011), using their relativistic accretion disk model BHSPEC to fit X-ray spectra when the source was in various spectral states, put some constraints on the BH mass. They showed that the inclination (i) has a strong influence on both the mass and the spin (a^*) of the BH derived by the model. Due to degeneracies in their best-fit parameters, they were only able to give a range of possible BH masses from 3000 $M_\odot$ (where the limit corresponds to $i = 0°$, (L_X/L_{Edd}) = 0.7, and $a^* = -1$) to $3 \times 10^5 M_\odot$ (where the limit corresponds to $i = 90°$ and $a^* = 0.99$). However, the inclination is likely to be less than 60°–70° due to the lack of observed eclipse dips assuming HLX-1 is a binary system. These results were obtained neglecting the effects of radial advection that are important at luminosities above the Eddington limit L_{Edd} with $L_{Edd} = 1.3 \times 10^{38}(M/M_\odot)$ erg s^{-1}. Radial advection is a

mechanism enabled to stabilize disks in the super-Eddington accretion regime (see, e.g., Abramowicz et al. 1988). This regime is reached when the accretion rate ($\dot{M}$) is larger than $\dot{M}_{Edd} = \eta^{-1}(L_{Edd}/c^2)$ with c being the speed of light and η being the radiation efficiency. In this regime, the vertical disk structure could be geometrically thick ($H/R > 0.5$ with H and R being the scale height and the radius of the disk, respectively). However, for a range of moderate super-Eddington $\dot{M}$-values there are still disk solutions for which the vertical disk structure can be considered as relatively thin. They are often referred to as slim disk solutions (Abramowicz et al. 1988). For large accretion rates ($\dot{m} \geqslant 10$ with $\dot{m} = (\dot{M}c^2/L_{Edd})$), electron scattering (opacity and Comptonization) has several effects on the emergent spectra: (1) they can be highly distorted and no longer look like a multi-color blackbody (BB) spectrum (e.g., Kawaguchi 2003, hereafter K03); (2) the $L \propto T^4$ relation with T being the color temperature at the inner disk radius for a standard α-disk (Shakura & Sunyaev 1973) is no longer valid (see Fukue 2000; K03). In addition, slim disks may extend beyond the innermost stable circular orbit (ISCO) due to non-negligible pressure support resulting in higher disk temperatures (e.g., Abramowicz et al. 1988, 2010; Watarai et al. 2000).

In this paper, we make use of the K03 disk model in order to: (1) investigate the accretion flow and BH properties in HLX-1 through spectral fitting of a multi-epoch and multi-instrument data set using a model that computes a wide range of sub- and super-Eddington accretion disk solutions; (2) investigate whether radial advection and electron scattering have important effects on the emergent spectra; (3) compare our results with those performed on less luminous ULXs using the same model that always favored critical or super-Eddington accretion onto a stellar mass BH (e.g., Yoshida et al. 2010; Foschini et al. 2006; Vierdayanti et al. 2006; Okajima et al. 2006).

The paper is organized as follows. In Section 2, we describe the data used to perform the spectral analysis together with the data reduction. Section 3 presents some possible observational evidence for effects of radial advection and/or electron scattering as well as the detection of possible X-ray lines. In Section 4,

Table 1
Log of the *XMM-Newton*, *Chandra*, and *Swift* Observations

Obs. Name	Instrument	Obs. ID	Start Date	End Date	Good Time (ks)
XMM1	*XMM-Newton* EPIC-pn	0204540201	2004 Nov 23	2004 Nov 23	22
XMM2	*XMM-Newton* EPIC-pn,	0560180901	2008 Nov 28	2008 Nov 28	51
XMM2	*XMM-Newton* RGS1, RGS2	0560180901	2008 Nov 28	2008 Nov 28	51
XMM3	*XMM-Newton* EPIC-pn	0655510201	2010 May 14	2010 May 15	62
Chandra	*Chandra* ACIS	13122	2010 Sep 6	2010 Sep 7	10
⋯	*Swift*–XRT	00031287(001-139)	2008 Oct 24	2011 Oct 10	360

we present the fitting results obtained with the K03 disk model. In Section 5, we discuss the implications of the fitting results on the BH mass, the accretion rate, and the disk structure. The main conclusions are given in Section 6.

2. OBSERVATION LOG AND DATA REDUCTION

We consider X-ray data coming from three observatories: *XMM-Newton*, *Chandra* (ACIS), and *Swift*. The data used in this study cover the different spectral states observed during the outbursts of HLX-1 (see Table 1). We used the same *XMM-Newton* and *Chandra* spectra as those presented in Servillat et al. (2011). The nomenclature used here is the same as that in Servillat et al. (2011) and Farrell et al. (2009) for the *XMM-Newton* data (see Table 1). For the *XMM-Newton* data, we only used the EPIC-pn data because they offer the best statistics for a given observation. Please refer to Servillat et al. (2011) for the details of the data reduction on the *XMM-Newton* and *Chandra* data. In order to investigate for the presence of X-ray lines during the outbursts, we also used the Reflection Grating Spectrometer (RGS) data from the XMM2 observation (see Table 1). The RGS data have been reduced using the standard *XMM-Newton* Science Analysis Software task RGSPROC and the most recent calibration files released in 2011 February. For the spectral analysis, we only considered the first order of the RGS data.

All the *Swift*–XRT photon counting data were processed using HEASOFT v6.11 and the latest calibration files (CALDB version 3.8). This new CALDB includes a new gain file enabled to correct the data for charge traps that accumulate on the CCD due to radiation damage (see Pagani et al. 2011). These traps can induce some energy offsets. The data were processed using the tool XRTPIPELINE v0.12.6. We inspected all segments of data to search for epochs when the background was enhanced by the presence of hot pixels induced by a high CCD temperature ($T > -55°$). For these time intervals, we checked whether there were some hot pixels in the extraction regions used to extract the spectra. Thus, we excluded the data from segments 00031287125 (0.8 ks) and 00031287129 (0.2 ks) because the data were severely contaminated by hot pixels due to a high ($T > -51°C$) CCD temperature. We also excluded the first orbit (∼0.6 ks) of segment 00031287023 for the same reason. These latter bad data induce an artificially high count rate in the X-ray light curve at MJD = 55,209 (during the P1 outburst—see Figure 1). However, the re-flare event seen around that time is not due to hot pixel contamination. We used the grade 0–12 events, giving slightly higher effective area at higher energies than the grade 0 events, and a 20 pixel (47.2 arcsec) radius circle to extract the source and background spectra using XSELECT v2.4b. The background extraction region was chosen in order to be close to the source extraction region and not to contain any *XMM-Newton* sources. The ancillary

response files were generated using XRTMKARF v0.5.9 and exposure maps generated by XRTEXPOMAP v0.2.7. The response file swxpc0to12s6_20010101v012.RMF is used to fit the spectra. To extract the *Swift*–XRT spectra, we divided the data over different intensity ranges for the outbursts P0, P1, and P2. As the work on the first three outbursts had been completed before the most recent outburst P3, we decided to compare the latest outburst with the previous three by dividing the data over time instead. Table 2 summarizes the nomenclature used for the *Swift*–XRT data.

3. SPECTRAL ANALYSIS

All the spectra were grouped at a minimum of 20 counts per bin to provide sufficient statistics to use the χ^2 minimization technique. The XMM3, *Swift*–XRT, and *Chandra* spectra were fitted in the 0.3–10 keV energy range within XSPEC v12.7.0 (Arnaud 1996), while the XMM1 and XMM2 spectra were fitted in the 0.2–10 keV energy range. The *Chandra* data, being moderately piled up, were fitted using the PILEUP model (Davis 2001) within XSPEC with a frame time fixed at 0.8 s (see Servillat et al. 2011 for more details). For each model, we determined the appropriate value of the grade morphing parameter. For the data used in this paper, the statistical errors are dominant over the instrumental systematics. The RGS1 and RGS2 spectra were binned at twice the resolution of the instrument ($\Delta\lambda = 0.2$ Å). Since with this choice of binning there are fewer than 20 counts per resolution bin, we used the *C*-statistic (Cash 1979) available within XSPEC for the spectral fit.

The total column density was fixed at the best-constrained value of $N_H = 4 \times 10^{20}$ cm^{-2} from the XMM2 observation (see Farrell et al. 2009). The Galactic absorption column in the direction of the source is equal to 1.8×10^{20} cm^{-2} (e.g., Kalberla et al. 2005). For all fits, the absorption is modeled using the WABS photoelectric absorption model. With a source redshift of 0.0224 (Wiersema et al. 2010), we adopted a source distance of $d_L = 95$ Mpc using the cosmological parameters from the *WMAP*5 results ($H_0 = 71$ km s^{-1} Mpc^{-1}, $\Omega_M = 0.27$, and $\Omega_\Lambda = 0.73$). All the errors quoted below are given at a 90% confidence level for one parameter of interest (i.e., $\Delta\chi^2 = 2.706$).

3.1. Hardness–Intensity Diagram

We fitted the *Swift*–XRT spectrum using a multi-color disk DISKBB and/or POWERLAW model. This phenomenological model is often used to fit the spectra of GBHBs. In that context, the power-law component is often interpreted as emission produced by a corona of hot electrons located in the inner regions of the accretion disk, while the DISKBB component is interpreted as the emission from the accretion disk (see Remillard & McClintock 2006). The photon index of the

Table 2
Nomenclature of the *Swift*–XRT Spectra

Spectrum Name	Comment
S_{1p}	Time when the source reached its maximum luminosity
	for the first outburst P1 (a count rate of CR > 0.02 counts s^{-1})
S_{2p}	Same but for the second outburst P2 (CR > 0.02 counts s^{-1})
S_{1p+2p}	Sum of the S_{1p} and S_{2p} spectra
$S_{\mathrm{after}2p}$	∼7 days after the peak of the second outburst P2 (CR > 0.02 counts s^{-1})
S_{CR0}	0.01 < CR < 0.02 counts s^{-1}
S_{CR1}	0.015 < CR < 0.02 counts s^{-1}
S_{CR2}	0.01 < CR < 0.015 counts s^{-1}
S_{CR3}	0.004 < CR < 0.01 counts s^{-1}
S_{CR4}	0.002 < CR < 0.004 counts s^{-1}
S_{CR5}	CR < 0.002 counts s^{-1}
$P3^-$	Outburst in 2011 Aug (55,788 < MJD < 55,809)
$P3^+$	Outburst in 2011 Aug (55,710 < MJD < 55,844)
S_{t1}	55,788 < MJD < 55,802
S_{t2}	55,803 < MJD < 55,822
S_{t3}	Re-flare event in the P3 outburst (55,826 < MJD < 55,844)

Table 3
Summary of the Spectral Parameters when Fitting the *Swift*–XRT Data Using the DISKBB Model

(1) Name[a]	(2) kT	(3) N_{BB}	(4) Γ	(5) N_Γ	(6) HR	(7) L_{tot}	(8) L_{disk}	(9) $\log(L_{\mathrm{bol}})$	(10) χ^2/dof
S_{1p+2p}	0.24 ± 0.01	20^{+6}_{-5}	...	...	0.06 ± 0.01	12.0 ± 0.4	12.0 ± 0.4	42.2 ± 0.03	42/36
S_{1p}	0.24 ± 0.02	20^{+8}_{-6}	...	...	0.06 ± 0.01	12.0 ± 0.5	12.0 ± 0.5	$42.19^{+0.04}_{-0.05}$	18/21
S_{2p}	0.22 ± 0.02	30^{+14}_{-10}	...	...	$0.04^{+0.01}_{-0.02}$	13.3 ± 0.7	13.3 ± 0.7	$42.23^{+0.05}_{-0.06}$	24/15
$S_{\mathrm{after}2p}$	0.18 ± 0.02	71^{+58}_{-33}	...	...	$0.022^{+0.006}_{-0.008}$	13.3 ± 0.8	13.3 ± 0.8	42.25 ± 0.07	54/67
S_{CR0}	$0.18^{+0.02}_{-0.01}$	36^{+14}_{-12}	$2.2^{+0.5}_{-0.6}$	$2.9^{+1.8}_{-1.4}$	$0.20^{+0.04}_{-0.06}$	$7.5^{+0.3}_{-0.6}$	$5.6^{+0.3}_{-0.6}$	41.90 ± 0.04	54/67
S_{CR3}	0.17 ± 0.05	11^{+36}_{-8}	$2.2^{+0.5}_{-0.6}$	1.8 ± 1.5	0.37 ± 0.15	$3.3^{+0.4}_{-0.8}$	$2.0^{+0.3}_{-0.7}$	$41.46^{+0.10}_{-0.13}$	54/67
S_{CR4}	...	...	$2.2^{+0.5}_{-0.6}$	2.0 ± 0.7	$1.2^{+0.9}_{-0.5}$	1.3 ± 0.2	...	...	54/67
S_{CR5}	...	...	$2.2^{+0.5}_{-0.6}$	$0.3^{+0.3}_{-0.2}$	1.2 ± 0.9	0.20 ± 0.06	...	...	54/67
S_{CR1}	0.18 ± 0.02	41^{+25}_{-19}	2.2^{b}	2.9 ± 1.2	$0.15^{+0.08}_{-0.06}$	$9.7^{+0.9}_{-1.6}$	$7.8^{+0.8}_{-1.5}$	42.03 ± 0.06	45/51
S_{CR2}	0.17 ± 0.02	40^{+27}_{-17}	2.2^{b}	3.0 ± 0.7	$0.22^{+0.06}_{-0.07}$	$6.7^{+0.7}_{-0.8}$	$4.8^{+0.3}_{-0.5}$	41.85 ± 0.06	45/51
S_{t1}	0.20 ± 0.02	39^{+25}_{-15}	...	...	$0.029^{+0.012}_{-0.010}$	12.4 ± 2.0	12.4 ± 2.0	42.22 ± 0.07	15.2/15
S_{t2}	0.20 ± 0.02	41^{+16}_{-12}	...	...	$0.023^{+0.006}_{-0.008}$	10.5 ± 1.0	10.5 ± 1.0	42.15 ± 0.05	17.2/22
S_{t3}	0.18 ± 0.03	44^{+57}_{-25}	2.2^{b}	$2.8^{+1.9}_{-2.0}$	$0.18^{+0.13}_{-0.08}$	8.6 ± 1.7	6.8 ± 1.2	41.98 ± 0.10	9.5/7

Notes. Columns: (1) spectrum name; (2) inner disk temperature in units of keV; (3) the blackbody normalization; (4) photon index of the power-law component; (5) normalization of the power law in units of 10^{-5} photons keV^{-1} cm^{-2} s^{-1}; (6) hardness ratio defined as the ratio of the observed 1.5–10 keV flux over the observed 0.3–10 keV flux; (7) unabsorbed 0.2–10 keV total luminosity in units of 10^{41} erg s^{-1}; (8) unabsorbed 0.2–10 keV disk luminosity in units of 10^{41} erg s^{-1}; (9) logarithm of the unabsorbed 0.01–20 keV disk luminosity in units of 10^{41} erg s^{-1}; (10) χ^2-value and number of degrees of freedom.
[a] See Table 2 for the nomenclature of the different spectra.
[b] Fixed parameter.

power law was tied together for the $S_{\mathrm{CR0,1,2,3,4,5}}$ spectra because we found Γ-values consistent within the errors when fitting the spectra individually. The power-law normalization and the parameters of the DISKBB model were left free to vary independently between spectra. The $S_{t1,2}$ spectra are well fitted by an absorbed DISKBB model. We did not obtain a good fit (χ^2/dof = 14.5/8) using an absorbed DISKBB model for the S_{t3} spectrum. There are residuals left at high energies. When adding a power-law component with Γ free, the Γ parameter was not constrained. So, we decided to freeze this parameter at the same value as found for the $S_{\mathrm{CR0,1,2,3,4,5}}$ spectra (Γ = 2.2). The fit is improved ($\Delta\chi^2 = 5$ for 1 dof, i.e., an improvement at a $>2\sigma$ significance level). For each spectrum, we then computed the hardness ratio (HR) of the 0.3–1.5 keV observed flux over the 1.5–10 keV flux. This is different from the *Swift* HR presented in

Godet et al. (2009) and Servillat et al. (2011) that was based on count rate. The HR values, the best-fit spectral parameters, and the 0.2–10 keV unabsorbed luminosity ($L = 4\pi d_L^2 F$ with F the 0.2–10 keV unabsorbed flux) for each spectrum are summarized in Table 3.

Figure 2 shows the *Swift*–XRT HR versus the 0.2–10 keV unabsorbed luminosity. The points from the *Chandra* ($kT = 0.21 \pm 0.01$ keV and $N = 37^{+11}_{-8}$), XMM2 ($kT = 0.17 \pm 0.01$ keV, $N = 40^{+16}_{-10}$, Γ = 2.1 ± 0.4, and $N_\Gamma = 1.9^{+0.8}_{-0.6} \times 10^{-5}$ photons cm^{-2} s^{-1} keV^{-1}) and XMM3[10] (Γ = $2.2^{+0.4}_{-0.6}$ and

---

[10] We also added a MEKAL component with $kT = 0.44^{+0.16}_{-0.12}$ keV to take a possible contamination from the galaxy into account (see Servillat et al. 2011). Only the power-law component was used to compute the hardness ratio.
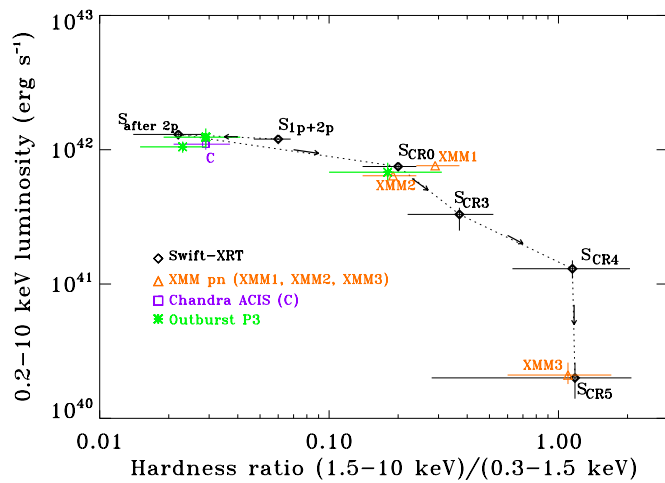
Figure 2. *Swift*–XRT hardness vs. intensity diagram. The *XMM-Newton* (triangles) and *Chandra* (square) points are also reported on the diagram. The arrows indicate the evolution from the peak to the end of the outbursts.

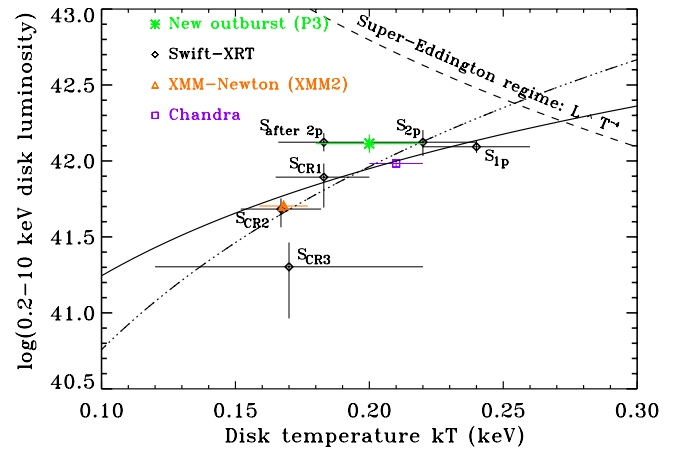(A color version of this figure is available in the online journal.)

Figure 3. Evolution of the unabsorbed 0.01–20 keV disk luminosity with the disk temperature. The values for *Swift* (diamonds), *XMM-Newton* (XMM2: triangles in orange), and *Chandra* (square in blue) are shown on the plot. The thick dot-dashed line corresponds to the best fit obtained using the $L \propto T^4$ relation, while the thick solid line corresponds to the best fit obtained using the $L \propto T^\alpha$ relation with $\alpha \sim 2.4$. The thick dashed line corresponds to the $L \propto T^{-4}$ prediction in the super-Eddington regime (Fukue 2000; King 2009).

(A color version of this figure is available in the online journal.)

$N_\Gamma = 2.9 \pm 0.7 \times 10^{-6}$ photons cm^{-2} s^{-1} keV^{-1}) observations are also reported on the plot.

Figure 2 shows that we have a good agreement between the different instruments. The HLX-1 track in the hardness–intensity diagram (HID) is clearly reminiscent of that observed in GBHBs. Between S_{1p+2p} and $S_{\text{after2}p}$, there is a softening of the source at nearly constant luminosity ($\sim 1.2 \times 10^{42}$ erg s^{-1}). Such a track in the HID is observed in GBHBs (see, e.g., Meyer-Hofmeister et al. 2009). However, the situation appears to be different because the disk temperature near the peak of the outbursts P1, P2, and P3 varies at nearly constant luminosity (from 0.24 ± 0.02 keV to 0.18 ± 0.02 keV—see Table 3). Note that if we consider the 3σ errors on the temperature (i.e., $\Delta\chi^2 = 9$ for one parameter of interest), then we find that all data have consistent kT-values given the limited statistical quality of the X-ray data used. However, when merging the S_{1p} and S_{2p} spectra (S_{1p+2p}) and the S_{t1} and S_{t2} spectra (S_{t1+t2}), the kT-values ($kT = 0.240^{+0.023}_{-0.020}$ for S_{1p+2p} and $kT = 0.20^{+0.019}_{-0.017}$ for S_{t1+t2}) are no longer consistent within the 3σ errors.

3.2. Investigating the L–T Relation

Figure 3 displays the disk temperature versus the unabsorbed 0.2–10 keV luminosity. We fitted our $L–kT$ points using a $L \propto T^a$ relation, where a was left as a free parameter. We obtained a good fit with $\log(L) = (2.4 \pm 0.7) \log T + 43.7 \pm 0.5$ (1σ errors). Feng & Kaaret (2007) showed that the luminosity L varies as $L \propto T^{-3.1\pm0.5}$ in the ULX NGC 1313 X-2. Using a larger sample of ULXs, Kajava & Poutanen (2008) found a $L \propto T^{-4}$ relation. King (2009) suggested that the $L \propto T^{-4}$ relation is expected in the super-Eddington regime provided that the geometrical beaming factor varies as $b \propto \dot{m}^{-2}$. From Figure 3, the observed trend in the $L–kT$ space does not follow such a correlation. Mizuno et al. (2001) found that some ULXs do present a $L \propto T^2$ relation. They interpreted such a correlation as a possible signature for moderate super-Eddington accretion (see also Fukue 2000; K03). However, we cannot exclude a T^4 relationship at the 3σ level (see also Servillat et al. 2011). In Figure 3, we also show the best fit obtained using the $L \propto T^4$ relation.

3.3. Evidence for Possible Line Features

When fitting the S_{1p+2p} spectrum, we found some strong residuals around 0.6 keV (see the top left panel in Figure 4). There may be some lower significance residuals at higher energy as well. We separately investigated the S_{1p} and S_{2p} spectra, and both show some residuals around 0.6 keV, in particular for S_{2p}. Given that the residuals are close to the instrumental oxygen edge, we investigated if the residual may have an instrumental origin. We extracted a background spectrum using different parts of the field of view and encompassing the time when the source was at the peak. The fit of the background spectrum does not reveal any residuals around the O edge. We checked the images and found no evidence of contamination by hot pixels. When the observations were performed the source location on the CCD was not close to the bad columns. The application of the charge trap correction did not change the residuals. So, the residuals are unlikely to be instrumental. We added a Gaussian line redshifted at the galaxy distance ($z = 0.0224$) with an intrinsic width equal to zero, because this parameter is otherwise not constrained. The fit was improved by $\Delta\chi^2 = 12.7$ for 2 dof. The line centroid is equal to $0.618^{+0.045}_{-0.042}$ keV and the equivalent width is EW $= 93^{+75}_{-51}$ eV (see the top right panel in Figure 4). The disk parameters do not change with $kT = 0.25 \pm 0.01$ keV and $N = 16^{+6}_{-4}$ (see Table 3 for a comparison). In the rest of the paper, we did not include the Gaussian line when fitting the S_{1p+2p} spectrum because it did not change the spectral parameters of the K03 disk model considered in Section 4 significantly.

In order to further investigate the soft X-ray emission at ~ 0.6 keV, we inspected the RGS data available from the XMM2 observation. Because the RGS1 and 2 spectra are background dominated below 0.5 keV and above 1.3 keV, we only considered this energy range in our analysis. In the 0.5–1.3 keV energy band a total of 1230 and 1170 counts were collected in the RGS1 and RGS2, respectively (with 520 and 605 net counts). We first used an absorbed DISKBB plus a power-law component to fit the data, fixing the photon index of the power-law component and the absorbing column density to the values derived from the XMM2 data (Farrell et al. 2009; Servillat et al. 2011). We found a temperature ($kT = 0.19 \pm 0.02$ keV) consistent with
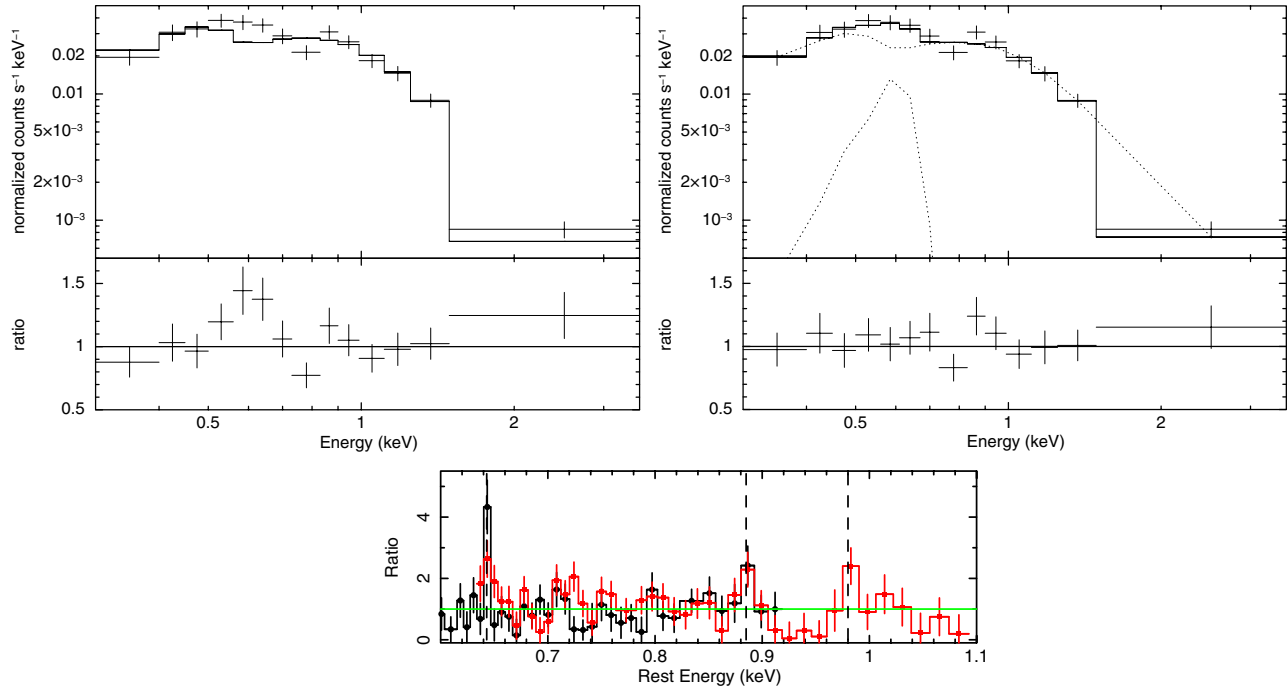
Figure 4. X-ray lines present in the *Swift*–XRT and *XMM-Newton* RGS data. Top: *Swift*–XRT spectrum when the source luminosity was at peak for the first and second outbursts (S_{1p+2p}). Left: using only an absorbed DISKBB model. Right: same model with the addition of a Gaussian line redshifted at the galaxy redshift ($z = 0.0224$). The dotted lines correspond to the different components of the model. Bottom: ratio of the RGS 1 (red) and RGS2 (black) spectra from the XMM2 observation over the model (an absorbed DISKBB + power-law model). The vertical dashed lines correspond to the centroids of the detected emission lines.

(A color version of this figure is available in the online journal.)

that derived from the EPIC data (see Table 3; see also Farrell et al. 2009; Servillat et al. 2011). Although the fit is statistically acceptable (C-statistic $= 160.4$ for 113 bins) a first inspection of the RGS1 and 2 residuals (see the bottom panel in Figure 4) reveals that features are present at $\sim$0.6 keV, $\sim$0.9 keV, and $\sim$1 keV.

We then added to the baseline continuum three unresolved Gaussian emission lines redshifted at the galaxy distance. The improvement in the fit due to the addition of the $\sim$0.6 keV emission line is $\Delta C/\mathrm{dof} = 26.2/2$ (corresponding to a detection significance >99.9% confidence). The emission line is detected at an energy centroid of $E = 0.642 \pm 0.002$ keV, a flux of $F = (1.91 \pm 0.6) \times 10^{-5}$ photons cm^{-2} s^{-1}, and an equivalent width of EW $= 20 \pm 7$ eV. The energy centroid is consistent with that derived from the *Swift*–XRT data, and the line equivalent width seems to decrease with the luminosity of the continuum. An additional line is detected at $E = 0.880^{+0.008}_{-0.002}$ keV ($\Delta C/\mathrm{dof} = 12.2/2$) with a flux of $F = (0.93 \pm 0.6) \times 10^{-5}$ photons cm^{-2} s^{-1} (EW $= 27 \pm 12$ eV). Finally, the addition of the third Gaussian line at $E = 0.98 \pm 0.01$ keV (EW $= 31 \pm 22$ eV) gave a much lower statistical significance ($\Delta C/\mathrm{dof} = 7.0/2$). Even if additional data are needed to further investigate the origin of these lines, we speculate that the most likely identification for the $\sim$0.6 keV and $\sim$0.9 keV lines is O VIII Lyα and Fe XVIII–Fe XIX. The third line, if any, might be associated with Ne X Lyα.

4. INVESTIGATING THE ACCRETION DISK STRUCTURE

4.1. A Simple Approach

In order to investigate whether the $L_X \propto T^{\sim 2.4}$ relation we found in Section 3.2 could be the result of a slim disk surrounding the BH, we first used the DISKPBB model instead of the DISKBB model. The DISKPBB model is a multi-temperature BB

Table 4
Summary of the *p*-value Derived Using the DISKPBB Model for the *XMM-Newton*, *Swift*–XRT, and *Chandra* Data

Spectrum	p
XMM1	$0 < 0.54$
XMM2	$0.63^{+0.37}_{-0.11}$
Chandra[a]	$0.57^{+0.33}_{-0.07}$
S_{1p}	0.71 ± 0.2
S_{2p}	$0.53 - 1$
$S_{\mathrm{after}2p}$	$0.55^{+0.45}_{-0.05}$
S_{CR0}	$0.7^{+0.3}_{-0.2}$

Note. [a] The value was obtained fixing N_H to 4×10^{20} cm^{-2}.

disk model where local disk temperature is given by $T(r) \propto r^{-p}$ with p a free parameter (e.g., Mineshige et al. 1994; Hirano et al. 1995; Watarai et al. 2000). When $p = 0.75$, the model is equivalent to a DISKBB model. For $p < 0.75$, radial advection starts to become important (e.g., Fukue 2000). Since the spectral shape of the model could change significantly with the *p*-value, we fitted the XMM1 and XMM2 spectra as well as those from *Swift* and *Chandra*. The XMM3 spectrum was not considered because any evidence for a disk component is only marginal (see Servillat et al. 2011). The results are summarized in Table 4. In most cases, the *p*-values are not well constrained. So we cannot tell from this model whether or not radial advection plays a role.

4.2. The Kawaguchi (2003) Disk Model

4.2.1. Description of the Model

Kawaguchi (2003) computed disk spectra in a self-consistent way, taking into account the effects of electron scattering

(opacity and disk Comptonization) and the effects of the relativistic correction (i.e., gravitational redshift and transverse Doppler shift) on the disk effective temperature in the inner part of the accretion disk. Not considering Doppler boosting implies that disk solutions are mostly seen face-on ($i = 0°$). The model table of the disk spectra,[11] from sub- to super-Eddington accretion rates with BH masses of 1–$10^3 M_\odot$, was successfully used for analysis of several ULXs (e.g., Foschini et al. 2006; Vierdayanti et al. 2006; Okajima et al. 2006; Yoshida et al. 2010). We used here a new table including additional computation for higher BH masses, extending up to $10^5 M_\odot$. The key parameters of the model are the BH mass (M), the accretion rate ($\dot{M}$), and the viscosity parameter (α). For sub-Eddington accretion rates (i.e., in the case of the standard disk), the emergent disk spectra are α-insensitive. Near and at super-Eddington rates, however, the disk spectra become α-sensitive because electron scattering, which is density sensitive (and density is α-sensitive), begins to affect the emergent spectra quite strongly. The normalization is fixed using the source distance ($d = 95$ Mpc). To perform the fits, we considered the model option 7 that takes into account the effects of advection, electron scattering on opacity, Comptonization, and relativistic effects (see Appendix A.1 for more details about the influence of the different model options on the spectral parameters from HLX-1 data). It is important to keep in mind that the K03 code automatically computes at each radius how much advection is present for a given accretion rate. All the models are computed assuming a non-rotating BH.

4.2.2. Results

To avoid calibration uncertainties between instruments affecting the fits (see Tsujimoto et al. 2011), we decided to fit the spectra from *XMM-Newton*, *Chandra*, and *Swift* separately.

We first fitted the *Swift*–XRT spectra S_{1p+2p}, $S_{\text{after}2p}$, S_{CR0}, and S_{CR3} by tying together the BH mass between them. We proceeded in the same way with the viscosity parameter α, while the accretion rate was left as an independent parameter between the different spectra. For the S_{CR0} and S_{CR3} spectra, we added a power-law component of which the photon index was tied together between the two spectra. This is because we found consistent values when fitting the two spectra individually. When we fixed the α-value to the default K03 model ($\alpha = 0.01$) we did not obtain a good fit because some spectra display strong residuals. In order to reproduce the spectra, it was necessary to leave the viscosity parameter α free. We then obtained a good fit ($\chi^2/\text{dof} = 108/104$). The best-fit parameters are given in Table 5. The derived BH mass is $M = 1.8^{+0.2}_{-0.1} \times 10^4 M_\odot$. Fitting the data from the outburst P3 using the K03 disk model, we found $M = 1.9^{+1.9}_{-0.2} \times 10^4 M_\odot$. These estimates are consistent and well inside the IMBH mass range. We note that the power-law component was not needed to obtain a good fit for the S_{t3} spectrum when leaving the viscosity parameter free to vary. Leaving the N_{H}-value free to investigate the sensitivity of the BH mass with respect to the N_{H} value did not change the spectral parameters much and they are still consistent within the errors with the values derived with $N_{\text{H}} = 4 \times 10^{20}$ cm^{-2}. Indeed, we found $N_{\text{H}} = 6.5^{+3.8}_{-2.5} \times 10^{20}$ cm^{-2} and $M = 2.8^{+1.7}_{-0.9} \times 10^4 M_\odot$ from the outbursts P0–P2, while we found $N_{\text{H}} = 4.1^{+2.8}_{-2.7} \times 10^{20}$ cm^{-2} and $M = 1.9^{+3.2}_{-0.6} \times 10^4 M_\odot$ from the outburst P3.

---

[11] http://heasarc.nasa.gov/xanadu/xspec/models/slimdisk.html

Second, we fitted the *Chandra* spectrum. For the K03 disk model, we estimated for the PILEUP model a grade morphing parameter of 0.33. Note that this parameter does not have a strong impact on the spectral parameters derived here. The derived BH mass is $M = 1.9 \pm 0.2 \times 10^4 M_\odot$. We then left the N_{H}-value free and we found $N_{\text{H}} = 3.7^{+3.9}_{-2.5} \times 10^{20}$ cm^{-2} and a BH mass estimate ($M = 1.8^{+1.0}_{-0.4} \times 10^4 M_\odot$) consistent with those derived from *Swift*.

Even if Farrell et al. (2009) showed that the XMM1 spectrum is well fitted by a steep power law ($\Gamma \sim 3.4$), suggesting that the source was in the steep power-law state as seen in some GBHBs, we decided to fit the XMM1 spectrum as well as the XMM2 one with the K03 disk model. This is because the emergent spectrum from the K03 disk model can have a shape strongly different from that of a simple multi-color disk spectrum (see Appendix A.1). We tied the BH mass between the two spectra, but we left α and $\dot{M}$ to vary independently. First, we keep N_{H} fixed at 4×10^{20} cm^{-2}. For XMM2, it was necessary to add a power-law component to obtain a good fit, while the addition of a power law for XMM1 did not improve the fit. The derived BH mass is then $M = 1.4 \pm 0.1 \times 10^4 M_\odot$, which is not consistent with the *Swift*–XRT and *Chandra* estimates within the 90% errors. If we consider the 3σ errors, then the estimates from the different instruments are all consistent within the errors. Then, in order to investigate the sensitivity of the BH mass with respect to the N_{H}-value, we left the N_{H} parameter free. We obtained a value of $N_{\text{H}} = 5.5^{+1.1}_{-1.0} \times 10^{20}$ cm^{-2} and a BH mass of $M = 1.9^{+1.3}_{-0.3} \times 10^4 M_\odot$. The photon index of the power-law component in both cases is consistent within the 90% errors between the *XMM-Newton* and *Swift*–XRT spectra. The best-fit results are given in Table 5.

For XMM1, the accretion rate ($\dot{m} \sim 4.4$) and a luminosity that is very different from that derived using a power law ($L \sim 1.3 \times 10^{42}$ erg cm^{-2}, a luminosity which was observed at the peak of the three outbursts) are commensurate with the values found for the XMM2 and S_{CR0} spectra (see Table 5). This, however, implies a large value of $\alpha = 0.13 \pm 0.07$, even if all α-values are consistent within the 3σ errors. If we force the viscosity parameter to the lowest possible value of the K03 model ($\alpha = 0.01$) keeping the mass fixed at $M = 1.8 \times 10^4 M_\odot$ and N_{H} free, we did not obtain a good fit ($\chi^2/\text{dof} = 47.3/24$). The addition of a power law improves the fit ($\chi^2/\text{dof} = 23.3/22$), but in this case the power-law component dominates over the disk component. In this case, we found similar Γ- and N_{H}-values to those given in Farrell et al. (2009).

5. DISCUSSION

5.1. Constraints on the BH Mass

To be able to derive a dynamical measurement of the BH mass in HLX-1 will be very challenging given the distance of the source. So we have to rely on indirect estimates such as spectral fitting of the X-ray data. Zampieri & Roberts (2009) showed that the BH mass estimate derived using spectral fitting can be highly variable depending on the disk model used (see their Table 2). In the case of HLX-1, Davis et al. (2011) used their advanced relativistic disk model to fit spectra with different shapes. They found a BH mass within the IMBH range (from $3000 M_\odot$ to $3 \times 10^5 M_\odot$) with extreme and opposite assumptions. In this paper, we used the K03 disk model to fit X-ray spectra of HLX-1 when the source was in various spectral states. We note that this model includes spectra for a wide range

Table 5
Summary of the Spectral Parameters when Fitting the *XMM-Newton*, *Swift*, and *Chandra* Data Using the Kawaguchi (2003) Disk Model

(1) Spectrum	(2) N_H	(3) M	(4) $\dot{M}$	(5) α	(6) Γ	(7) N_Γ	(8) L_{tot}	(9) L_{disk}	(10) χ^2/dof^a
XMM1	4	1.4 ± 0.1	4.8 ± 0.3	$0.11^{+0.08}_{-0.05}$	...	...	$4.2^{+0.2}_{-0.6}$	$4.2^{+0.2}_{-0.6}$	283/215
XMM2	4	1.4 ± 0.1	5.9 ± 0.4	$0.010^{+0.002}_{-0.000}$	$1.6^{+0.3}_{-0.4}$	1.0 ± 0.4	$5.1^{+0.1}_{-0.3}$	$4.3^{+0.1}_{-0.2}$	283/215
XMM1	$5.5^{+1.1}_{-1.0}$	$1.9^{+1.3}_{-0.3}$	$4.4^{+0.3}_{-0.5}$	0.13 ± 0.07	...	...	$4.9^{+0.2}_{-0.6}$	$4.9^{+0.2}_{-0.6}$	277/214
XMM2	$5.5^{+1.1}_{-1.0}$	$1.9^{+1.3}_{-0.3}$	$5.4^{+0.5}_{-0.7}$	$0.010^{+0.005}_{-0.000}$	$1.8^{+0.4}_{-0.5}$	$1.3^{+0.4}_{-0.6}$	$5.7^{+0.1}_{-0.5}$	$4.9^{+0.1}_{-0.3}$	277/214
Chandra	4	1.9 ± 0.2	$10.2^{+0.8}_{-2.1}$	$0.025^{+0.009}_{-0.015}$	...	...	$10.7^{+0.3}_{-0.4}$	$10.7^{+0.3}_{-0.4}$	38/28
Chandra	$3.7^{+3.9}_{-2.5}$	$1.8^{+1.0}_{-0.4}$	$10.2^{+0.7}_{-2.7}$	$0.023^{+0.017}_{-0.013}$	...	...	$10.5^{+0.5}_{-0.6}$	$10.5^{+0.5}_{-0.6}$	37.6/27
S_{1p+2p}	4	$1.8^{+0.2}_{-0.1}$	$10.1^{+0.3}_{-2.3}$	$0.05^{+0.04}_{-0.02}$	...	...	$11.0^{+0.4}_{-0.7}$	$11.0^{+0.4}_{-0.7}$	108/104
$S_{after2p}$	4	$1.8^{+0.2}_{-0.1}$	$10.5^{+0.3}_{-1.1}$	$0.015^{+0.005}_{-0.005}$	...	...	$9.9^{+4.2}_{-0.3}$	$9.9^{+4.2}_{-0.3}$	108/104
S_{CR0}	4	$1.8^{+0.2}_{-0.1}$	5.5 ± 0.5	$0.020^{+0.009}_{-0.006}$	$1.7^{+0.6}_{-0.8}$	$1.4^{+1.6}_{-0.9}$	$6.2^{+0.3}_{-0.7}$	$5.1^{+0.2}_{-0.4}$	108/104
S_{CR3}	4	$1.8^{+0.2}_{-0.1}$	3.8 ± 0.4	0.01 fixed	$1.7^{+0.6}_{-0.8}$	$1.6^{+1.5}_{-1.0}$	$3.3^{+0.6}_{-0.7}$	2.3 ± 0.5	108/104
S_{CR1}	4	1.8 fixed	7.1 ± 0.9	$0.016^{+0.028}_{-0.006}$	$1.6^{+0.9}_{-1.3}$	$1.3^{+2.5}_{-1.0}$	$8.0^{+0.5}_{-0.9}$	$6.9^{+0.4}_{-0.8}$	46/50
S_{CR2}	4	1.8 fixed	$4.9^{+0.3}_{-0.5}$	$0.019^{+0.024}_{-0.009}$	$1.6^{+0.9}_{-1.3}$	$1.3^{+2.5}_{-1.1}$	$5.5^{+0.4}_{-0.6}$	$4.4^{+0.4}_{-0.5}$	46/50
S_{t1}	4	1.8 fixed	$10.9^{+0.3}_{-1.5}$	$0.01^{+0.11}_{-0.00}$	...	...	10.8 ± 1.1	10.8 ± 1.1	37.7/41
S_{t2}	4	1.8 fixed	9.1 ± 1.0	$0.016^{+0.005}_{-0.006}$	...	...	8.8 ± 0.6	8.8 ± 0.6	37.7/41
S_{t3}	4	1.8 fixed	$6.7^{+1.4}_{-1.2}$	$0.018^{+0.023}_{-0.007}$	...	...	6.7 ± 0.9	6.7 ± 0.9	37.7/41

Notes. Columns: (1) spectrum name; (2) absorption column in units of 10^{20} cm^{-2}; (3) BH mass in units of 10^4 $M_\odot$; (4) accretion rate in units of L_{Edd}/c^2 with L_{Edd} and c, the Eddington limit and the speed of light, respectively; (5) viscosity parameter; (6) photon index of the power-law component; (7) normalization of the power law in units of 10^{-5} photons keV^{-1} cm^{-2} s^{-1}; (8) unabsorbed 0.3–10 keV total luminosity in units of 10^{41} erg s^{-1}; (9) unabsorbed 0.3–10 keV disk luminosity in units of 10^{41} erg s^{-1}; (10) χ^2-value and number of degrees of freedom.
[a] The *Swift*-XRT, *XMM-Newton* EPIC-pn, and *Chandra*/ACIS data were fitted separately. For a given instrument, we fitted together all the available spectra or a subset of them.

of accretion rates from sub- to super-Eddington rates. In all cases for ULXs, the fits favored super- or near-Eddington accretion onto a stellar mass BH. However, the fits to HLX-1 spectra do favor an IMBH solution with a BH mass of $M = 1.8^{+1.6}_{-0.5} \times 10^4$ $M_\odot$. This is an interesting result because we get three independent and nonetheless consistent mass estimates from three different instruments (*Swift*–XRT, *XMM-Newton* EPIC-pn, and *Chandra*/ACIS) and over different spectral shapes. This estimate is consistent with the observational lower and upper limits on the BH mass (Farrell et al. 2009; Servillat et al. 2011). So, using the K03 model which assumes a non-spinning BH and a face-on accretion disk, we find that an IMBH solution is favored with an estimated mass of $\sim 1.8 \times 10^4$ $M_\odot$. The BH accretes at the Eddington limit ($\dot{m} \sim 10$) and radiates close to the Eddington luminosity at the outburst peak ($L_{Edd} = 2.3^{+2.0}_{-0.6} \times 10^{42}$ erg s^{-1}). This corresponds to an Eddington fraction of $f_{Edd} = 1.1^{+0.6}_{-0.5}$ considering a bolometric luminosity of 2.5×10^{42} erg s^{-1} on average (see Figure 5).

5.2. Comparison with the Results from Davis et al. (2011)

Using their BHSPEC model, Davis et al. (2011) studied the dependency of the BH mass in HLX-1 on the inclination and the BH spin. We can only compare our results with their work for $a^* = 0$ and $i = 0°$. In that configuration, they found a consistent mass estimate for XMM2 and *Chandra* with $\log M \sim 3.8 \pm 0.1$ (S. W. Davis 2011, private communication). However, no solution could be found in this case for the *Swift* spectra, because the $f_{Edd} = L_X/L_{Edd}$ ratio was pegged to the maximum permitted value in their BHSPEC model (i.e., $f_{Edd} = 1$; S. W. Davis 2011, private communication). From Figures 2, 5, and 6 in Davis et al. (2011), the best-fit contours for fixed inclination in the a^* versus $\log M$ plots overlap well with
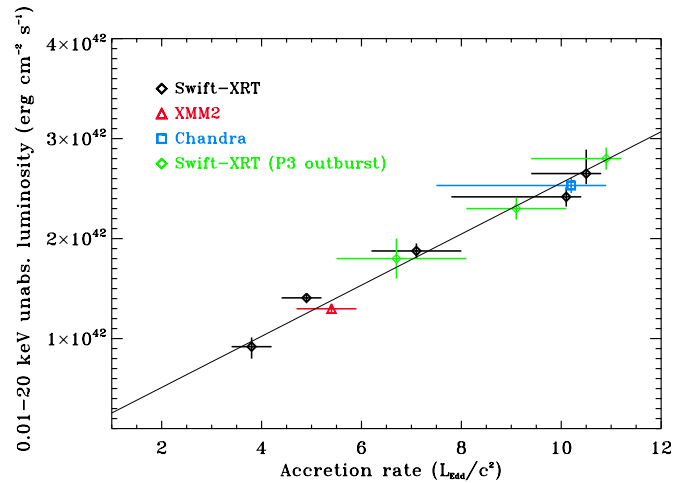

Figure 5. Linear correlation between the 0.01 and 20 keV unabsorbed luminosity derived using the Kawaguchi (2003) slim disk model and the accretion rate. The luminosity was computed using the following relation: $L_{bol} = 4\pi d_L^2 F_{bol}$ with F_{bol}, the bolometric unabsorbed flux and $d_L = 95$ Mpc.
(A color version of this figure is available in the online journal.)

the simulations for the range of allowed parameters. Thus, they found a consistent mass estimate between the three instruments for $i = 0°$ and $a^* = 0.7$ with $\log M \sim 4.0$ for *Swift* and *Chandra* and $\log M \sim 3.9$ for XMM2. The mass values derived by Davis et al. (2011) from the XMM2 and *Chandra* spectra for $a^* = 0$ and $i = 0°$ are smaller than the one derived using the K03 disk model. We note that the Eddington ratios (f_{Edd}) they obtained are large (and close to 1). From our fitting results using the K03 model, we found similar high f_{Edd} values near the outburst peak. We believe that for such high f_{Edd} values the effects of advection on the emergent spectra should be considered.

Evaluating the level of systematic errors of the K03 model by comparison with alternative models by exploring the whole parameter space is beyond the scope of the present paper and deserves a dedicated paper. Nevertheless, we estimated the level of systematic errors of the K03 model by comparison with the KERRBB (Li et al. 2005) and BHSPEC models assuming a non-spinning BH ($a^* = 0$) and a face-on disk ($i = 0°$) in the limit of low mass accretion rate (i.e., a few percent of the Eddington limit). In that limit, the accretion disk is expected to be very close to the relativistic model of Novikov & Thorne (1973). We found that the level of systematic errors in the BH mass between the K03 and KERRBB models is less than 45% when only considering the relativistic effects in both models (see Appendix A.2). When comparing the results between the K03 and BHSPEC models taking into account the relativistic effects and the effects due to Comptonization and electron scattering, we found that the level of systematic errors in the BH mass is less than 24% (see Appendix A.2). In all cases, the values of the accretion rate derived using the K03, KERRBB, and BHSPEC models agree within the errors. So, providing we have a similar level of systematic errors over the whole parameter space, we are confident that our BH mass and accretion rate estimates are reliable.

5.3. The Disk Structure

Figure 5 shows a linear correlation between the 0.01–20 keV bolometric disk luminosity (L) and the accretion rate so that $L = \eta \dot{m} L_{\rm Edd}$ with radiation efficiency $\eta = 0.11 \pm 0.03$. Watarai et al. (2000) found a similar linear correlation for $\dot{m} < 20$. This implies that advection does not play a significant role, and that the slim disk solutions are not needed. At all times during the outbursts, the disk aspect ratio H/R is less than 0.2, from Figure 5 in K03. Note that H/R is mostly independent of the BH mass and the viscosity parameter.

From Figure 1 in K03, the disk appears to be radiation pressure dominated in its inner regions for all the $\dot{m}$-values found. Such disks might be viscously and thermally unstable, and they might give rise to outbursts (Taam & Lin 1984; Honma et al. 1991; Lasota & Pelat 1991; Xue et al. 2011). However, Hirose et al. (2009) showed via MHD simulations that such disks could be thermally stable (but see Xue et al. 2011). Most observations of Galactic X-ray binaries in outburst radiating above 10% of the Eddington luminosity for a stellar mass BH do not show any evidence for such an instability except perhaps for GRS 1915+105 (Belloni et al. 1997; Xue et al. 2011).

5.4. The Evolution of the Accretion Rate

Figure 6 shows the evolution of the accretion rate through the different outbursts. At the peak of the three outbursts and for a few weeks ($\sim$3 and $\sim$2–3 weeks for the outbursts P2 and P3, respectively), the BH accretes at the Eddington limit ($\dot{m} \sim 10$). This "plateau" is seen in the X-ray light curve of the outbursts P2 and P3 (see the right panel in Figure 1). Recently, Lasota et al. (2011) proposed that the HLX-1 outbursts may be due to enhanced mass-transfer rate onto a pre-existing accretion disk when an asymptotic giant branch star orbiting along an eccentric orbit with a period of $\sim$1 year passing at periastron is tidally stripped. Such a mechanism is known to produce "plateaus" in light curves (Bath & Pringle 1981; Esin et al. 2000). The latter authors considered an unstable disk that became stable after an enhanced mass-transfer rate phase. In the case of HLX-1, the situation is different since the disk is stable.
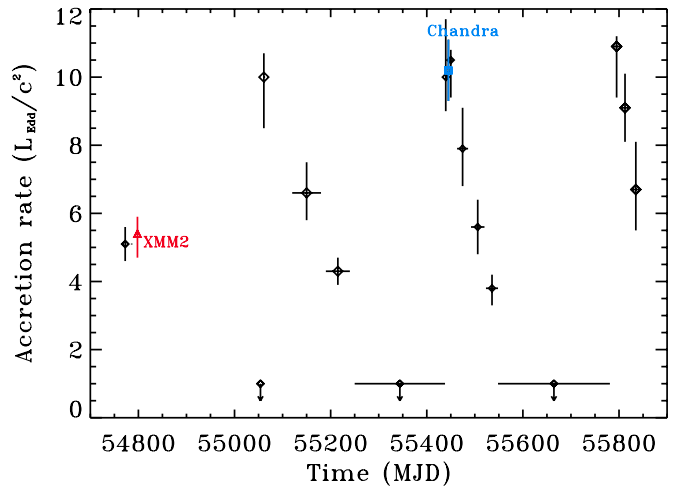

Figure 6. Evolution of the accretion rate over time.
(A color version of this figure is available in the online journal.)

Therefore, a quasi-constant enhanced mass-transfer rate during a given time interval would naturally produce a "plateau" in the light curve. After the "plateau," the accretion rate drops exponentially with a decay time of 182 ± 30 days and 92 ± 15 days for the outbursts P1 and P2, respectively. The difference in the decay time is because there was a small re-flare event at the end of the outburst P1 (see Figure 1). From the evolution of the accretion rate over time, we calculated the mass accreted during the outbursts P1 and P2 assuming that the accretion rate is the same throughout the disk. If this is not the case, then the values derived below are lower limits. We found an accreted mass of $\sim$1.2 × 10^{-4}$ $M_\odot$ and $\sim$8.2 × 10^{-5}$ $M_\odot$ for the outbursts P1 and P2, respectively.

At the end of the outbursts P1 and P2, i.e., when the source undergoes a transition from the high/soft state to the low/hard state, the count rate drops very quickly over a timescale less than a month (see Figure 1). As shown by Servillat et al. (2011), any disk component in the spectrum of HLX-1 in the low/hard state is marginal. Given the XMM3 luminosity of $\sim$2 × 10^{40}$ erg s^{-1} derived from the power-law component and assuming a radiation efficiency in the low/hard state of 0.11 as during the outbursts, we could compute an upper limit on the accretion rate in the low/hard state of $\dot{m} < 0.09$, i.e., $\dot{M} < 3.6 × 10^{-6}$ $M_\odot$ yr^{-1}. This is nicely consistent with the results obtained by Esin et al. (1997, 1998) using the advection-dominated accretion flow model. According to that model, this must be connected with a varying (receding) inner disk radius (e.g., Dubus et al. 2001). Higher statistical quality of the data when the source transits to the low/hard state will be needed to further investigate that possibility.

5.5. The L–T Relation

In the luminosity–temperature space, we found a correlation $L \propto T^{\sim 2.4}$. Fukue (2000) and Kawaguchi (2003) showed that near the Eddington limit ($\dot{m} = 10$) and above a departure from the L–T^4 relation is expected, due to the change of the radial profile of the disk temperature and the $\dot{m}$-sensitive disk color temperature via the effects of electron scattering. However, below this limit the disk is still expected to follow the $L \propto T^4$ relation found in the standard disk model. Apart from the peak of the outbursts when the accretion rate is at the Eddington limit, the accretion rate is below this limit. Therefore, we should expect

to have a $L \propto T^4$ correlation. The behavior near the peak is probably responsible for the flatter correlation. To check that, we fitted our L–kT points for the XMM2, S_{CR1}, S_{CR2}, S_{CR3}, and S_{t3} observations (for which $\dot{m} < 10$—see Table 5) using the relation for a standard disk. We found: $\log(L) = 4 \log T + 44.95 \pm 0.06$ (1σ error). From Equation (1) in Lasota et al. (2011) giving L as a function of the color disk temperature at the inner disk radius and the BH mass, we derived the following relation: $\log(L) \sim 4 \log T + 45.1$ using $\eta \sim 0.11$, $M = 1.8 \times 10^4\ M_\odot$, and $R_{ISCO} = 3\,R_S$ (for a non-rotating BH). This demonstrates that the disk in HLX-1 follows the $L \propto T^4$ relation.

6. CONCLUSION

We investigated in detail the X-ray spectral properties of the best IMBH candidate, HLX-1, using multi-epoch data collected by three different X-ray instruments (*Swift*–XRT, *XMM-Newton* EPIC-pn, and *Chandra*). To do so, we used the K03 disk model in order to constrain the BH mass, the accretion rate, and the disk structure in a non-biased way. Indeed, this disk model has the advantage of taking into account the effects of radial advection and covering a wide range of accretion rates (from sub- to super-Eddington) assuming a non-rotating BH and a face-on disk inclination ($i = 0°$). We found that our multi-epoch data are consistent with sub-Eddington accretion onto a nearly $2 \times 10^4\ M_\odot$ BH. At the peak, the X-ray luminosity is near the Eddington luminosity. The derived radiation efficiency is $\eta \sim 11\%$. The disk solution we found for HLX-1 is different from those derived for other ULXs using the same disk model (e.g., Vierdayanti et al. 2006; Okajima et al. 2006; Yoshida et al. 2010). Indeed, for other ULXs the spectral fitting favors super- or near-Eddington accretion onto a stellar mass BH. Here, the disk in HLX-1 likely undergoes sub- and near-Eddington accretion onto an IMBH and appears to stay relatively thin. The inner regions of the accretion disk are dominated by radiation pressure. We also showed that the source follows the $L \propto T^4$ relation globally. At the outburst peak and for a further few days, the BH accretes at near the Eddington limit ($\dot{m} \sim 10$, i.e., $\sim 4 \times 10^{-4}\ M_\odot\ yr^{-1}$). The occurrence of this "plateau" at the outburst peaks could provide some evidence that the outburst mechanism is driven by enhanced mass-transfer rate onto a pre-existing accretion disk as proposed by Lasota et al. (2011). After the "plateau," the accretion rate decreases exponentially until the end of the outburst. However, it is not clear from our data what is the geometry of the accretion flow when the source transits to the low/hard state, even if the presence of an optically thin advection-dominated flow would avoid a dramatic variation in the accretion rate by more than two orders of magnitude from the peak to the low/hard state. Finally, the recent outburst starting in 2011 August gives more credit to the ~ 1 year recurrence timescale proposed by Lasota et al. (2011). Our dedicated multi-wavelength (radio, optical, and X-ray) observations of this outburst will shed further light on the nature of this unique source as well as on the outburst mechanism.
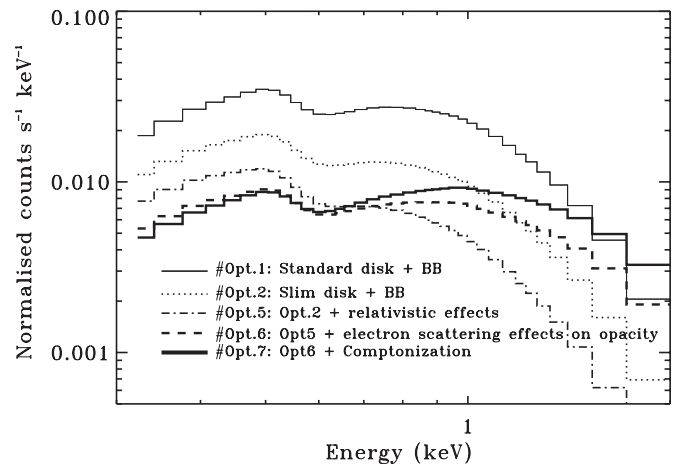
Figure 7. Evolution of the spectral shape of the Kawaguchi (2003) disk model when adding different physical components to an initial standard disk model. The latter model was obtained fitting the S_{1p+2p} spectrum.

APPENDIX

A.1. Impact of the K03 Disk Model Computing Options on the Shape of the Emergent Spectra, the BH Mass, and the Accretion Rate

The K03 model makes use of different options to compute the emergent spectra starting from a local BB and then including different physical effects (advection, electron opacity, relativistic effects, and Comptonization). First, we investigate the impact of these different options on the shape of the emergent spectra as well as on the M and $\dot{M}$ parameters. We take the example of the S_{1p+2p} spectrum as an illustration, but what is described below is also valid for the other spectra.

Figure 7 shows the modification of the S_{1p+2p} spectrum when selecting different model options: (1) standard disk and local BB; (2) slim disk and local BB; (5) slim disk including relativistic effects on the BB; (6) slim disk including the effects of electron scattering on opacity and relativistic effects; (7) slim disk including the effects of electron scattering on opacity, Comptonization, and relativistic effects. Here, the term "slim disk" implies that the K03 code automatically computes (at each radius) how much advection is present for a given accretion rate.

First, we just changed the option parameters without running a new fit for option 1 in order to see the effects of the different model components. When using option 1, we got for the S_{1p+2p} spectrum a BH mass around $1.8 \times 10^3\ M_\odot$ and $\dot{m} \sim 32$ assuming a viscosity parameter of $\alpha = 0.01$. Such high $\dot{m}$-values mean super-Eddington accretion. However, in this case radial advection is expected to start playing a significant role. The large derived $\dot{M}$-value also implies that electron opacity and Comptonization should play an important role (see Figure 2 in Kawaguchi 2003, for instance). This results in more spectral boosting toward high energies. In order to obtain the global shape of the data when including all the above effects in a slim disk (option 7), it is clear that the effects of both electron scattering on opacity and Comptonization have to be reduced.

Table 6
Evolution of the Parameters of the Kawaguchi ([2003](#)) Slim Disk Model for
Different Model Options

Option (1)	M (2)	$\dot{m}$ (3)	α (4)	χ^2/dof (5)
1	$1.8^{+0.4}_{-0.2}$	$32.2^{+1.1}_{-5.6}$	0.01 fixed	40.4/36
2	$3.5^{+0.3}_{-0.2}$	$38.0^{+1.4}_{-1.3}$	$0.82^{+0.18}_{-0.55}$	40.1/35
5	$2.3^{+1.0}_{-0.6}$	200^{+477}_{-101}	>0.26	51.59/35
6	29^{+4}_{-14}	$10.0^{+1.7}_{-0.9}$	$0.14^{+0.01}_{-0.04}$	67.21/35
7	18 ± 2	$10.1^{+0.3}_{-2.3}$	$0.05^{+0.06}_{-0.02}$	43.4/35

Notes. The fits were performed using the S_{1p+2p} spectrum with $N_H = 4 \times 10^{20}$ cm^{-2}. Columns: (1) computation option from the Kawaguchi ([2003](#)) slim disk model (see Section A.1); (2) BH mass in units of $10^3 \, M_\odot$; (3) accretion rate in units of L_{Edd}/c^2; (4) viscosity parameter; (5) value of the χ^2 and number of degree of freedom.

Table 7
Evolution of the Parameters of the Kawaguchi ([2003](#)) Slim Disk Model for
Different Model Options Forcing the Source Distance to 3.5 Mpc Instead of
the Measured Distance of 95 Mpc

Option (1)	M (2)	$\dot{m}$ (3)	α (4)	χ^2/dof (5)
1	79^{+15}_{-12}	$1.07^{+0.05}_{-0.04}$	0.01 fixed	40.2/36
2	64^{+15}_{-10}	$1.7^{+0.2}_{-0.2}$	0.01 fixed	40.3/36
5	58^{+14}_{-8}	$2.9^{+0.4}_{-0.5}$	0.01 fixed	40.8/36
6	52^{+5}_{-5}	$3.3^{+0.1}_{-0.1}$	0.01 fixed	40.4/36
7	122^{+13}_{-10}	$1.4^{+0.1}_{-0.1}$	0.01 fixed	42/36

Notes. Columns: (1) computation option from the Kawaguchi ([2003](#)) slim disk model (see Section A.1); (2) BH mass in units of $M_\odot$; (3) accretion rate in units of L_{Edd}/c^2; (4) viscosity parameter; (5) value of the χ^2 and number of degree of freedom.

To do so, the accretion rate (in units of the Eddington rate) has to decrease, which in turn results in an increase of the BH mass.

To check this, we fitted the S_{1p+2p} spectrum for each chosen option leaving the model parameters free. The evolution of the model parameters are summarized in Table 6. From option 1 to option 2, there is a relatively small variation of the M and $\dot{m}$ parameters ($M \sim 3.4 \times 10^3 \, M_\odot$ and $\dot{m} \sim 38$). From option 2 to option 5 (including the relativistic effects), we obtained a significant impact on the accretion rate ($\dot{m} \sim 200$) and a slight decrease of the BH mass ($M \sim 2.3 \times 10^3 \, M_\odot$). Given the large accretion rate ($\dot{m} \sim 38$) derived in option 2, the accretion disk extends below the last stable orbit (e.g., Watarai et al. [2000](#)). The relativistic effects (gravitational redshift and transverse Doppler redshift) when applying option 5 strongly suppress the emission coming from these regions, which in turn results in the model underestimating the data. To have a good match between the data and the model, the accretion rate has to be increased. From option 5 to option 6, the spectral parameters significantly change with an increase in the BH mass by one order of magnitude and a decrease of the accretion rate by more than one order of magnitude. From option 6 to option 7, the parameters do not change significantly ($M \sim 1.8 \times 10^4 \, M_\odot$ and $\dot{m} \sim 10$).

From option 5, the accretion flow is in the super-Eddington regime. The effects of Comptonization and electron scattering (option 6) are likely to be significant given the large $\dot{m}$-value (see Figure 2 in K03). This would in turn result in a stronger hardening of the model than what is seen in Figure 7. However, in order to obtain a good fit given the shape of the S_{1p+2p} spectrum, the effects of both Comptonization and electron scattering have to be strongly minimized. This is achieved by significantly decreasing the accretion rate (the accretion flow is then in the sub-Eddington regime) and therefore by significantly increasing the BH mass. If we force the source distance from 95 Mpc (measured distance) to an arbitrary lower value (e.g., $d = 3.5$ Mpc), such a dramatic change in the BH mass and the accretion rate is not seen because the accretion flow always stays in the sub-Eddington regime (see Table 7).

A.2. Comparison of the K03, KERRBB, and BHSPEC Results in the Limit of the Novikov & Thorne ([1973](#)) Relativistic Disk Model

We compare the results from the K03 disk model with those obtained with KERRBB and BHSPEC assuming a non-spinning BH ($a^* = 0$) and a face-on disk ($i = 0°$) in the limit of low mass accretion rate (i.e., less than 10% of the Eddington limit).

In that limit, the accretion is expected to follow the predictions of the relativistic disk model of Novikov & Thorne ([1973](#)). In the K03 model, this limit corresponds to $\dot{m} \leqslant 1.6 L_{Edd}/c^2$. For the comparisons with KERRBB, we limit ourselves by setting the hardening factor to 1 in the model (i.e., we did not take the effects of electron scattering and Comptonization into account). We also did not consider the effects of limb darkening and self-irradiation since they are not included in the K03 disk model. This configuration corresponds to option 5 in the K03 disk model (only including the relativistic effects). For the comparisons with BHSPEC, we used the option 7 (including the effects for Comptonization and electron scattering) in the K03 disk model. We used the table of BHSPEC models bhspec_mass_0.01.fits[12] considering BH mass up to $300 \, M_\odot$.

To perform the comparisons, we proceeded in both cases as follows.

1. We fitted the S_{1p+2p} spectrum (i.e., when the source luminosity is maximum) using the WABS*KERRBB and WABS*BHSPEC model with $a^* = 0$, $i = 0°$, and $N_H = 4 \times 10^{20}$ cm^{-2} for different and arbitrary values of the source distance D so that the $\dot{m}$-values derived were below 10% of the Eddington limit.
2. From the best fits, we simulated a model spectrum with an exposure time of 38 ks using the *Swift*–XRT response files and the fakeit command in Xspec.
3. We fitted the faked spectra with the WABS*K03 model with α fixed to 0.01, the same source distance D as used for the KERRBB and BHSPEC fits and the options 5 and 7 when comparing the results with KERRBB and BHSPEC, respectively.

Tables 8 and 9 summarize the results of the comparisons with KERRBB and BHSPEC, respectively. From Table 8, we show that there is a systematic discrepancy (less than 45% in the range considered) in the BH mass between the two models, while the accretion rate values appear to be consistent within the errors. From Table 9, we obtain a good agreement between the BHSPEC and K03 models within the 3σ errors except for the BH mass estimate for a distance of 2.9 Mpc. Based on that latter case, the "systematic errors" in the BH mass are less than 24%. We also show in Tables 8 and 9 comparisons with $\dot{m}$-values larger than 10% of the Eddington limit. Again, we emphasize the good agreement between the K03-KERRBB models and K03-BHSPEC models. So, we conclude that the K03 disk model

---

[12] http://www.cita.utoronto.ca/~swd/xspec.html

Table 8
Summary of the Results Obtained for both the KERRBB and K03 Models

Distance (Mpc)	Parameter	KERRBB[a]	K03[b]	$\dot{m}$[c] (L_{Edd}/c^2)
10.	Mass ($M_\odot$)	145	191^{+42}_{-29} [d]	
10.	$\dot{m}$ (10^{19} g s^{-1})	21.6	$18.8^{+5.1}_{-3.8}$	$(6.8^{+1.1}_{-0.9})$
5.	Mass ($M_\odot$)	73	105^{+7}_{-8}	
5.	$\dot{m}$ (10^{19} g s^{-1})	5.4	$5.3^{+0.4}_{-0.4}$	$(3.5^{+0.1}_{-0.1})$
2.9	Mass ($M_\odot$)	42	52^{+9}_{-7}	
2.9	$\dot{m}$ (10^{19} g s^{-1})	1.8	$1.5^{+0.4}_{-0.3}$	$(2.0^{+0.3}_{-0.2})$
2.	Mass ($M_\odot$)	29	39^{+4}_{-3}	
2.	$\dot{m}$ (10^{19} g s^{-1})	0.85	0.75 ± 0.08 [d]	$(1.32^{+0.07}_{-0.07})$
1.5	Mass ($M_\odot$)	22	32^{+2}_{-5}	
1.5	$\dot{m}$ (10^{19} g s^{-1})	0.49	$0.50^{+0.04}_{-0.08}$	$(1.08^{+0.04}_{-0.03})$

Notes. The errors are given at the 90% confidence level.
[a] The effects of Comptonization, electron scattering, limb darkening, and self-irradiation were not taking into account.
[b] We used the option 5 in the K03 model that only includes the relativistic effects.
[c] Accretion rate value derived from the K03 disk model.
[d] Consistent at the 3σ level.

Table 9
Summary of the Results Obtained for both the BHSPEC and K03 Models

Distance (Mpc)	Parameter	BHSPEC	K03[a]	$\dot{m}$[b] L_{Edd}/c^2
7.	Mass ($M_\odot$)	234	237^{+73}_{-21}	
7.	$l = L_X/L_{Edd}$	0.146	$0.200^{+0.06}_{-0.04}$ [c]	$(3.20^{+0.06}_{-0.04})$
5.	Mass ($M_\odot$)	158	172^{+31}_{-23}	
5.	l	0.110	$0.116^{+0.024}_{-0.020}$	$(1.9^{+0.2}_{-0.2})$
2.9	Mass ($M_\odot$)	85	105^{+8}_{-8} [d]	
2.9	l	0.069	$0.073^{+0.006}_{-0.006}$	$(1.18^{+0.04}_{-0.04})$
2.	Mass ($M_\odot$)	54	55^{+6}_{-5}	
2.	l	0.051	$0.064^{+0.007}_{-0.006}$	$(1.02^{+0.03}_{-0.02})$ [e]

Notes. The errors are given at the 90% confidence level.
[a] We used the option 7 in the K03 model that includes the relativistic effects as well as the effects of Comptonization and electron scattering.
[b] Accretion rate value derived from the K03 disk model.
[c] Consistent at the 3σ level.
[d] Marginally consistent at 3σ.
[e] Lower error bar pegged to the lowest permitted value of the model ($\dot{m} = 1$).

provides reliable estimates of accretion disk parameters (mass and accretion rate).

REFERENCES

Abramowicz, M. A., Czerny, B., Lasota, J. P., & Szuszkiewicz, E. 1988, ApJ, 332, 646
Abramowicz, M. A., Jaroszyński, M., Kato, S., et al. 2010, A&A, 521, 15
Amaro-Seoane, P., & Santamaír, L. 2010, ApJ, 722, 1197
Arnaud, K. 1996, in ASP Conf. Ser. 101, Astronomical Data Analysis Software and Systems, ed. J. G. Barnes (San Francisco, CA: ASP), 17
Bath, G. T., & Pringle, J. E. 1981, MNRAS, 194, 967
Belloni, T., Mendez, M., King, A. R., van der Klis, M., & van Paradijs, J. 1997, ApJ, 488, L109
Bringmann, T., Lavalle, J., & Salati, P. 2009, Phys. Rev. Lett., 103, 1301
Cash, W. 1979, ApJ, 228, 939
Colbert, E. J. M., & Mushotzky, R. F. 1999, ApJ, 519, 89
Davis, J. E. 2001, ApJ, 562, 575
Davis, S. W., Narayan, R., Zhu, Y., et al. 2011, ApJ, 734, 111
Dubus, G., Hameury, J.-M., & Lasota, J.-P. 2001, A&A, 373, 251
Esin, A. A., Lasota, J.-P., & Hynes, R. I. 2000, A&A, 354, 987
Esin, A. A., McClintock, J. E., & Narayan, R. 1997, ApJ, 489, 865
Esin, A. A., Narayan, R., Cui, W., Grove, J. E., & Zhang, S.-N. 1998, ApJ, 505, 854
Evans, P. A., Beardmore, A. P., Page, K. L., et al. 2009, MNRAS, 397, 1177
Farrell, S. A., Webb, N. A., Barret, D., Godet, O., & Rodrigues, J. M. 2009, Nature, 460, 73
Feng, H., & Kaaret, P. 2007, ApJ, 660, 113
Fornasa, M., & Bertone, G. 2008, Int. J. Mod. Phys. D, 17, 1125
Foschini, L., Ebisawa, K., Kawaguchi, T., et al. 2006, Adv. Space Res., 38, 1378
Fukue, J. 2000, PASJ, 52, 829
Gao, Y., Wang, Q. D., Appleton, P. N., & Lucas, R. A. 2003, ApJ, 596, 171
Gladstone, J. C., Roberts, T. P., & Done, C. 2009, MNRAS, 397, 1836
Godet, O., Barret, D., Webb, N. A., Farrell, S. A., & Gehrels, N. 2009, ApJ, 705, L109
Godet, O., Farrell, S. A., Barret, D., Webb, N. A., & Servillat, M. 2011, ATel, 3569
Hirano, A., Kitamoto, S., Yamada, T. T., Mineshige, S., & Fukue, J. 1995, ApJ, 446, 350
Hirose, S., Krolik, J. H., & Blaes, O. 2009, ApJ, 691, 16
Honma, F., Matsumoto, R., & Kato, S. 1991, PASJ, 43, 147
Kajava, J. J. E., & Poutanen, J. 2008, in AIP Conf. Proc. 1054, COOL DISCS, HOT FLOWS: The Varying Faces of Accreting Compact Objects, ed. M. Axelsson (Melville, NY: AIP), 39
Kalberla, P. M. W., Burton, W. B., Hartmann, D., et al. 2005, A&A, 440, 775
Kawaguchi, T. 2003, ApJ, 593, 69
King, A. R. 2009, MNRAS, 393, 41
King, A. R., Davies, M. B., Ward, M. J., Fabbiano, G., & Elvis, M. 2001, ApJ, 552, 109
Lasota, J.-P., Alexander, T., Dubus, G., et al. 2011, ApJ, 735, 89
Lasota, J.-P., & Pelat, D. 1991, A&A, 249, 574
Li, L.-X., Zimmerman, E. R., Narayan, R., & McClintock, J. E. 2005, ApJS, 157, 335
Matsubayashi, T., Shinkai, H., & Ebisuzaki, T. 2004, ApJ, 614, 864
Meyer-Hofmeister, E., Liu, B. F., & Meyer, F. 2009, A&A, 508, 329
Micic, M., Holley-Bockelmann, K., Sigurdsson, S., & Abel, T. 2007, MNRAS, 380, 1533
Mineshige, S., Hirano, A., Kitamoto, S., Yamada, T. T., & Fukue, J. 1994, ApJ, 426, 308
Mizuno, T., Kubota, A., & Makishima, K. 2001, ApJ, 554, 1282
Novikov, I. D., & Thorne, K. S. 1973, in Black Holes, ed. C. DeWitt & B. S. DeWitt (New York: Gordon and Breach), 343
Okajima, T., Ebisawa, K., & Kawaguchi, T. 2006, ApJ, 652, 105
Pagani, C., Beardmore, A. P., Abbey, A. F., et al. 2011, A&A, 534, 20
Pakull, M. W., & Grisé, F. 2008, in AIP Conf. Proc. 1010, A POPULATION EXPLOSION: The Nature & Evolution of X-ray Binaries in Diverse Environments, ed. R. M. Bandyopadhyay, S. Wachter, D. Gelino, & C. R. Gelino (Melville, NY: AIP) 303
Remillard, R. A., & McClintock, J. E. 2006, ARA&A, 44, 49
Roberts, T. P. 2007, Ap&SS, 311, 203
Servillat, M., Farrell, S. A., Lin, D., et al. 2011, ApJ, 743, 6
Shakura, N. I., & Sunyaev, R. A. 1973, A&A, 24, 337
Strohmayer, T. E., & Mushotzky, R. F. 2003, ApJ, 586, 61
Taam, R. E., & Lin, D. N. C. 1984, ApJ, 287, 761
Trenti, M., & Stiavelli, M. 2007, ApJ, 667, 38
Tsujimoto, M., Guainazzi, M., Plucinsky, P. P., et al. 2011, A&A, 525, 25
Vierdayanti, K., Mineshige, S., Ebisawa, K., & Kawaguchi, T. 2006, PASJ, 58, 915
Watarai, K., Fukue, J., Takeuchi, M., & Mineshige, S. 2000, PASJ, 52, 133
Webb, N. A., et al. 2012, Science, submitted
Wiersema, K., Farrell, S. A., Webb, N. A., et al. 2010, ApJ, 721, L102
Xue, L., Sdowski, A., Abramowicz, M. A., & Lu, J.-F. 2011, ApJS, 195, 7
Yoshida, T., Ebisawa, K., Matsushita, K., Tsujimoto, M., & Kawaguchi, T. 2010, ApJ, 722, 760
Zampieri, L., & Roberts, T. P. 2009, MNRAS, 400, 677